The Astrophysical Journal, 927:189 (12pp), 2022 March 10 https://doi.org/10.3847/1538-4357/ac51d5
© 2022. The Author(s). Published by the American Astronomical Society.
OPEN ACCESS

Cold Gas in Massive Galaxies as a Critical Test of Black Hole Feedback Models

Jingjing Shi[1,2], Yingjie Peng[1], Benedikt Diemer[3], Adam R. H. Stevens[4,5], Annalisa Pillepich[6], Alvio Renzini[7], Jing Dou[8,9], Yu Gao[10,11], Qiusheng Gu[12,13], Luis C. Ho[1,14], Xu Kong[15,16], Claudia del P. Lagos[4,5], Di Li[17,18], Jiaxuan Li[1,19], Roberto Maiolino[20,21,22], Filippo Mannucci[23], Lizhi Xie[24], and Chengpeng Zhang[1,25,26]
[1] Kavli Institute for Astronomy and Astrophysics, Peking University, Beijing 100871, People's Republic of China; jingssrs1989@gmail.com, yjpeng@pku.edu.cn
[2] Kavli Institute for the Physics and Mathematics of the Universe (WPI), The University of Tokyo Institutes for Advanced Study (UTIAS), The University of Tokyo, 5-1-5 Kashiwanoha, Kashiwa-shi, Chiba, 277-8583, Japan
[3] Department of Astronomy, University of Maryland, College Park, MD 20742, USA
[4] International Centre for Radio Astronomy Research, The University of Western Australia, Crawley, WA 6009, Australia
[5] Australian Research Council Centre of Excellence for All Sky Astrophysics in 3 Dimensions (ASTRO 3D), Australia
[6] Max-Planck-Institut für Astronomie, Königstuhl 17, D-69117 Heidelberg, Germany
[7] INAF - Osservatorio Astronomico di Padova, Vicolo dell'Osservatorio 5, I-35122 Padova, Italy
[8] Shanghai Astronomical Observatory, Chinese Academy of Sciences, 80 Nandan Road, Shanghai 200030, People's Republic of China
[9] University of Chinese Academy of Sciences, 19A Yuquan Road, Beijing 100049, People's Republic of China
[10] Department of Astronomy, Xiamen University, Xiamen, Fujian 361005, People's Republic of China
[11] Purple Mountain Observatory & Key Laboratory for Radio Astronomy, Chinese Academy of Sciences, 10 Yuanhua Road, Nanjing 210033, People's Republic of China
[12] School of Astronomy and Space Science, Nanjing University, Nanjing 210093, People's Republic of China
[13] Key Laboratory of Modern Astronomy and Astrophysics (Nanjing University), Ministry of Education, Nanjing 210093, People's Republic of China
[14] Department of Astronomy, School of Physics, Peking University, 5 Yiheyuan Road, Beijing 100871, People's Republic of China
[15] CAS Key Laboratory for Research in Galaxies and Cosmology, Department of Astronomy, University of Science and Technology of China, Hefei 230026, People's Republic of China
[16] School of Astronomy and Space Sciences, University of Science and Technology of China, Hefei 230026, People's Republic of China
[17] CAS Key Laboratory of FAST, National Astronomical Observatories, Chinese Academy of Sciences, Beijing 100012, People's Republic of China
[18] School of Astronomy and Space Science, University of Chinese Academy of Sciences, Beijing 100049, People's Republic of China
[19] Department of Astrophysical Sciences, 4 Ivy Lane, Princeton University, Princeton, NJ 08544, USA
[20] Cavendish Laboratory, University of Cambridge, 19 J.J. Thomson Avenue, Cambridge, CB3 0HE, UK
[21] Kavli Institute for Cosmology, University of Cambridge, Madingley Road, Cambridge, CB3 0HA, UK
[22] Department of Physics and Astronomy, University College London, Gower Street, London, WC1E 6BT, UK
[23] Istituto Nazionale di Astrofisica, Osservatorio Astrofisico di Arcetri, Largo Enrico Fermi 5, I-50125 Firenze, Italy
[24] Tianjin Normal Universisty, Binshuixidao 393, Tianjin, People's Republic of China
[25] George P. and Cynthia Woods Mitchell Institute for Fundamental Physics and Astronomy, Texas A&M University, College Station, TX 77843-4242, USA
[26] Department of Physics and Astronomy, Texas A&M University, College Station, TX 77843-4242, USA
Received 2021 August 9; revised 2021 December 19; accepted 2022 February 2; published 2022 March 15

Abstract

Black hole feedback has been widely implemented as the key recipe to quench star formation in massive galaxies in modern semianalytic models and hydrodynamical simulations. As the theoretical details surrounding the accretion and feedback of black holes continue to be refined, various feedback models have been implemented across simulations, with notable differences in their outcomes. Yet, most of these simulations have successfully reproduced some observations, such as the stellar mass function and star formation rate density in the local universe. We use the recent observation of the change in the neutral hydrogen gas mass (including both H_2 and H I) with the star formation rate of massive central disk galaxies as a critical constraint of black hole feedback models across several simulations. We find that the predictions of IllustrisTNG agree with the observations much better than the other models tested in this work. This favors IllustrisTNG's treatment of active galactic nuclei (AGN)—where kinetic winds are driven by black holes at low accretion rates—as more plausible among those we test. In turn, this also indirectly supports the idea that the massive central disk galaxy population in the local universe was likely quenched by AGN feedback.

Unified Astronomy Thesaurus concepts: Galaxies (573)

1. Introduction

Baryons cool and form stars within the potential well of dark matter halos (Rees & Ostriker 1977; White & Rees 1978; White & Frenk 1991). However, only 5%–25% of baryons within dark matter halos are converted into stars by $z = 0$ efficiently in most galaxies (Zheng et al. 2007; Dutton et al. 2010; Yang et al. 2009, 2012; Wang & Jing 2010; Kravtsov et al. 2018; Moster et al. 2018; Wechsler & Tinker 2018; Behroozi et al. 2019). Stellar feedback, such as supernova (SN) explosions and stellar winds, can heat up and even eject gas in low-mass systems, reducing their star formation efficiency (Larson 1974; White & Rees 1978; Silk 2003; Springel & Hernquist 2003). However, to suppress the SF efficiency in massive systems where the potential well is deeper, SN feedback alone is not enough (Benson et al. 2003). Active galactic nuclei (AGN) feedback is invoked as a necessary mechanism to reduce further SF activity in massive systems in galaxy formation and evolution models (Silk & Rees 1998; Bower et al. 2006; Croton et al. 2006; Yuan & Narayan 2014; Henriques et al. 2015; Yuan et al. 2015, 2018, see Somerville & Davé 2015 and Naab & Ostriker 2017 for a review on the current status of galaxy formation and evolution models).

Original content from this work may be used under the terms of the Creative Commons Attribution 4.0 licence. Any further distribution of this work must maintain attribution to the author(s) and the title of the work, journal citation and DOI.

AGN feedback is launched in quite different ways in different theoretical models of cosmological simulation and semianalytic models (SAMs). In general, the way that feedback is launched depends on the black hole (BH) accretion rate: the high-accretion-rate mode and low-accretion-rate mode. In SAMs (Bower et al. 2006; Croton et al. 2006; Guo et al. 2011; Henriques et al. 2015), BHs continue to accrete gas from the circumgalactic medium, the induced feedback injects thermal energy into the gas in the dark matter (DM) halo to effectively reduce the hot-gas cooling rate. In Illustris (Vogelsberger et al. 2013; Torrey et al. 2014) and IllustrisTNG (Weinberger et al. 2017; Pillepich et al. 2018b), when the BH accretion rate is higher than a certain threshold, the thermal energy is inserted into the surrounding gas within galaxies; when the BH accretion rate is lower, a hot bubble is injected (in Illustris) or a certain amount of kinetic energy is added to the gas surrounding the BH (so called "kinetic feedback", in IllustrisTNG). In the Evolution and Assembly of Galaxies and their Environments (EAGLE), a single heating mode from BH is launched, which nevertheless mimics the relatively quiescent "radio mode" and vigorous "quasar mode" when the BH accretion rate is much smaller than or similar to the Eddington rate (Crain et al. 2015; Schaye et al. 2015). Despite the nonnegligible differences among these implementations, they are all adjusted to reproduce the $z = 0$ stellar mass function and the stellar mass–BH mass scaling relation to various levels of agreement. More observations, especially those that are not implemented for model calibration, are needed to constrain the AGN feedback models in cosmological simulations and SAMs.

One promising constraint comes from investigating the gas content in galaxies. AGN feedback can act either negatively or positively (Cresci & Maiolino 2018). Negative AGN feedback is believed to suppress the SF in massive galaxies in two ways: through prevention (Cresci et al. 2015) and ejection. Preventative feedback is when the hot gas cannot cool efficiently due to the heating from AGN, while ejective feedback is when cold gas is pushed away from the galaxy due to the wind produced by the accreting BH (Zinger et al. 2020). The role of AGN feedback being preventive or ejective is not necessarily directly tied to how the feedback is implemented in practice. For example, the kinetic mode in IllustrisTNG can also be preventive, as kinetic energy can also transform into thermal energy via shocks (Weinberger et al. 2017); likewise, the thermal injection in EAGLE can produce gas ouflows (i.e., can be ejective too) due to the induced pressure gradients. By contrast, and of lesser importance, positive AGN feedback is when additional star formation is induced by the compression of molecular gas in a galaxy's disk (Silk 2013) or directly in the outflowing cold gas (Ishibashi & Fabian 2012; Zubovas et al. 2013; Maiolino et al. 2017; Gallagher et al. 2019). Understanding how AGN feedback impacts galaxies' gas and star formation properties can help us to distinguish/constrain various implementations in these models (Terrazas et al. 2020).

On average, passive galaxies unsurprisingly have less cold gas than star-forming ones (Saintonge et al. 2016; Catinella et al. 2018; Tacconi et al. 2018). However, when massive central disk galaxies ($10^{10.6} < M_\star/M_\odot < 10^{11}$) are selected, i.e., focusing on internal quenching mechanisms and excluding external environmental ones, Zhang et al. (2019; Z19 hereafter) found that, as SFR decreases, their H I gas mass remains surprisingly constant, but both H_2 gas mass and H_2 star formation efficiency decrease. Zhang et al. (2021; Z21 hereafter) further show the change of gas content is also accompanied by the rapid increase in the stellar concentration index, bulge-to-total mass ratio, central velocity dispersion, and AGN frequency (which in Z19 are mostly LINERs). These altogether suggest more massive black holes, and possibly stronger AGN feedback, in quenching or quenched galaxies. These results are robust against different SFR estimators, including the $H\alpha/D_{4000}$-based SFR (Brinchmann et al. 2004) with aperture correction by performing spectral energy distribution (SED) fitting to the photometry outside the fiber, and SFRs obtained from SED fitting of UV, optical, and mid-IR bands (Salim et al. 2016, 2018), see more detailed discussion in Z21. Since cold gas is the fuel of star formation and can provide direct evidence of how quenching may happen in galaxies, this observational result of massive central disk galaxies can be used as a new constraint for current galaxy formation and evolution simulations/models, especially for AGN feedback. In particular, as H_2 is mainly distributed in the inner stellar disk and H I is usually located at larger radii, the observed H I and H_2 versus SFR relations as in Z19 potentially put a strong observational constraint on the strength of AGN feedback and on its "inside-out" nature, as it needs to clear out most of the H_2 gas in the inner disk while retaining much of the H I gas in the outer disk.

In this work, we focus mainly on the prediction for the neutral hydrogen gas–SFR relation of massive central discs produced by IllustrisTNG, EAGLE, L-Galaxies, and Illustris. We show that IllustrisTNG agrees with the observed gas–SFR relation better than the others. We then study the gas distribution and quenching mechanism of the central discs in IllustrisTNG in more detail, as it may give useful clues on the quenching process in the real universe.

2. Data and Methods

2.1. The IllustrisTNG Simulation

The IllustrisTNG project (Marinacci et al. 2018; Naiman et al. 2018; Nelson et al. 2018; Pillepich et al. 2018a; Springel et al. 2018) is a suite of cosmological hydrodynamical simulations in a ΛCDM universe run with the moving-mesh code AREPO (Springel 2010). It contains simulations of three different volumes, TNG50, TNG100, and TNG300 with respective box lengths of $35\,h^{-1}$ Mpc, $75\,h^{-1}$ Mpc, and $205\,h^{-1}$ Mpc. In this work, we use the publicly available TNG100 data as a good balance between resolution and volume (Nelson et al. 2019b).[27] The numerical resolution of TNG100 is also closest to the test runs on which the free parameters of the subgrid physics were calibrated, which results in the best match with observational constraints (e.g., stellar mass function etc.). The IllustrisTNG galaxy formation and evolution model includes gas cooling and heating, star formation, stellar evolution and chemical enrichment, SN feedback, BH growth, AGN feedback, and cosmic magnetic field (see Weinberger et al. 2017; Pillepich et al. 2018b for more detailed information on the models).

Galaxies in TNG100 are identified using the Friends-of-Friends (FOF) and SUBFIND algorithms (Davis et al. 1985; Springel et al. 2001). The neutral gas fraction of non-star-forming gas cells is calculated self-consistently in the simulation by computing the cooling rate and photoionization

[27] https://www.tng-project.org

rate due to the UV background, while star-forming gas cells are modeled as a two-phase medium following Springel & Hernquist (2003), where the hot phase gas is assumed fully ionized and the cold phase gas fully neutral (see Appendix A1 of Stevens et al. 2019b for more information). In each gas cell, the molecular hydrogen fraction can be obtained by post-processing using empirical, simulation-based, or theoretical prescriptions. In this work, we use the molecular hydrogen gas fraction calculated using five different models (Diemer et al. 2018): the empirical model where the molecular gas fraction is found to be correlated with the midplane pressure (Leroy et al. 2008, L08 hereafter), the high-resolution chemical-network-inclusive simulations that produced calibrated relations between molecular gas fraction and surface density, metallicity, and UV field (Gnedin & Kravtsov 2011, GK11 hereafter; Gnedin & Draine 2014, GD14 hereafter), and analytical equilibrium models of molecular clouds with detailed calculations of molecular hydrogen creation and destruction (Krumholz 2013, K13 hereafter; Sternberg et al. 2014, S14 hereafter). Galaxies are rotated into a face-on position using the angular momentum of gas and stars, and the H I and H_2 fractions are computed using the projected quantities (such as surface density, SFR surface density). That is, we use the "map" methods of Diemer et al. (2018). We refer the readers to Diemer et al. (2018, 2019) and Stevens et al. (2019b, 2019a, 2021) for more details on the decomposition methods and comparison with observations (also see Davé et al. 2020 for an additional comparison with other hydrodynamic simulations).

In this work, $M_\star$ for each galaxy is calculated within the radius of $2R_\star$, where $R_\star$ is the stellar half-mass–radius. To approximate the scale of the Arecibo beamwidth (3.′4 at 21 cm; e.g., Jones et al. 2018) for the relevant galaxies in the Arecibo Legacy Fast Arecibo L-Band Feed Array (ALFALFA) survey, we only count the H I gas within a fixed radius of 70 kpc (i.e., the corresponding physical scale of the beamwidth at $z = 0.037$) as in Diemer et al. (2019) and Bahé et al. (2016); but see Stevens et al. (2019b) for a more precise method. We also test our results with fixed radii of 50 kpc and 80 kpc and see no significant variations of our results. We also count the H_2 gas within the radius of 70 kpc and test the results using the radius of 20 kpc (which roughly corresponds to the Institute for Radio Astronomy in the Millimeter Range (IRAM) aperture for the xCOLD GASS survey). Our results stay unchanged as H_2 is mainly located in the central region of galaxies. To make a direct comparison with the observed trend of cold gas content versus SFR as in Z19 and Z21, we apply the same selection criteria of massive central disk galaxies with $10^{10.6} < M_\star/M_\odot < 10^{11}$. We use the $\kappa_{\rm rot}$ parameter to distinguish disk galaxies from elliptical galaxies, defined as the ratio of the ordered rotation versus the total kinetic energy using stellar particles (Sales et al. 2012; Rodriguez-Gomez et al. 2015). If $\kappa_{\rm rot} > 0.5$, the galaxy is rotation-dominated, disk-like; if $\kappa_{\rm rot} < 0.5$, the galaxy is dispersion-dominated, elliptical-like. Figure A1 in Diemer et al. (2019) compared the elliptical galaxy fraction in TNG100 based on $\kappa_{\rm rot}$ with the observed fraction given by Calette et al. (2018), finding a good match between simulations and observations in the stellar mass range studied in this work. In Section 3 and Appendix A, we give more discussion on the morphology selection. With the above selection, our final sample in TNG100 includes 674 centrals, of which 340 are disk-like. The SFRs are obtained by averaging the star formation over the past 200 Myr within two different apertures: everything that are gravitationally self-bounded within the SUBFIND-identified subhalo, SFR(all grav.), and that within $2R_\star$, SFR($< 2R_\star$). We take SFR(all grav.) as our default choice. In Appendix B, we also test our results with SFR calculated using various apertures and timescales and find that the general trends remain similar.

Due to the finite mass resolution in the simulation, galaxies' SFRs suffer a resolution limit (see Donnari et al. 2019 for a detailed discussion). For SFRs averaged in the past 200 Myr, this SFR resolution limit is $10^{-2.46}\,M_\odot\,{\rm yr}^{-1}$. For galaxies with SFRs below this limit, we reassign each of them a random SFR between $10^{-2.8}$–$10^{-2.5}\,M_\odot\,{\rm yr}^{-1}$ so that they show up in the log-scale scatter plots.

2.2. L-Galaxies, EAGLE, and Illustris-1

L-Galaxies 2020 is a very recent version of the Munich semianalytic galaxy formation model (Henriques et al. 2020).[28] This model is built upon the subhalo merger trees from the Millennium and Millennium-II simulations scaled to first-year Planck cosmology. The evolution of baryonic components are traced in the model, including hot gas atmosphere, cold interstellar gas, a gas reservoir ejected by winds, stars in the bulge, disk, and intracluster light, and central supermassive BHs. Elemental abundances (including H) are traced in a galactic chemical enrichment scheme introduced by Yates et al. (2013). In this work, we select the central galaxies with $10^{10.6} < M_\star/M_\odot < 10^{11}$ and disk-to-total stellar mass ratios $({\rm D/T}) > 0.5$ from the publicly available online database.[29] The amount of hydrogen in cold-gas component gives us the neutral hydrogen mass. In a future work, we will also include the newest version of L-Galaxies (Ayromlou et al. 2021).

The EAGLE simulation (Crain et al. 2015; Schaye et al. 2015; McAlpine et al. 2016)[30] is a cosmological hydrodynamical simulation run with the smoothed particle hydrodynamics (SPH) solver GADGET3 with Planck cosmology. We use the largest-volume run, Ref-L100N1504, with a box length of 100 Mpc. Halos and galaxies are identified using the FOF and SUBFIND algorithms. Stochastic, isotropic heating of gas particles is implemented for SF feedback ($\Delta T_{\rm SF} = 10^{7.5}$K) and BH feedback ($\Delta T_{\rm BH} = 10^{8.5}$K), where $\Delta T_{\rm SF}$ and $\Delta T_{\rm BH}$ are the temperature jump of gas particles receiving feedback energy. The neutral hydrogen fractions of gas particles are estimated in postprocessing (Lagos et al. 2015; Bahé et al. 2016; Crain et al. 2017), using the fitting function of Rahmati et al. (2013), which is calibrated using TRAPHIC radiative transfer simulations (Pawlik & Schaye 2008). Davé et al. 2020 compared the atomic and molecular hydrogen content of galaxies from IllustrisTNG, EAGLE, and SIMBA (Davé et al. 2019); we refer the readers there for more information. Similar to TNG100, the massive central discs are selected using $\kappa_{\rm rot} > 0.5$. The neutral hydrogen mass are calculated within a radius of 60 kpc; however, the gas content stays roughly unchanged even with a different radius choice of 40 kpc.

The Illustris simulation is the precursor simulation of IllustrisTNG (Genel et al. 2014; Vogelsberger et al. 2014; Nelson et al. 2015; Sijacki et al. 2015).[31] In this work, we use Illustris-1, which has the same initial condition, volume, and resolution as TNG100. The main difference of Illustris, compared to

[28] https://lgalaxiespublicrelease.github.io/
[29] http://www.mpa-garching.mpg.de/millennium
[30] http://eagle.strw.leidenuniv.nl
[31] https://www.illustris-project.org

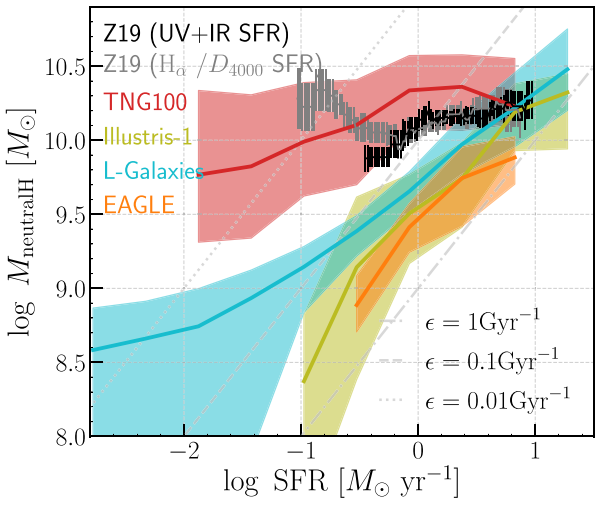

Figure 1. Neutral hydrogen (H I + H_2) mass vs. SFR for central disk galaxies ($10^{10.6} < M_\star/M_\odot < 10^{11}$) in TNG100 ($\kappa_{\mathrm{rot}} > 0.5$), Illustris ($\kappa_{\mathrm{rot}} > 0.5$), L-Galaxies (D/T > 0.5), and EAGLE ($\kappa_{\mathrm{rot}} > 0.5$). The black and gray lines show the observational results from Z19 for SFRs calculated using Hα emission and D_{4000} (corrected for the limited Sloan Digital Sky Survey (SDSS) fiber aperture) and UV+IR SEDs, respectively. The solid lines are the median relations, with the 16th–84th percentile ranges shown with the shaded regions. We also overplot lines of fixed star formation efficiency $\epsilon = \mathrm{SFR}/M_{\mathrm{gas}}$ for 1 Gyr^{-1}, 0.1 Gyr^{-1}, and 0.01 Gyr^{-1}.

IllustrisTNG, is the treatment of BH accretion and feedback (as discussed in Section 1) and of galactic winds. Illustris also lacks magnetohydrodynamics. The central discs in Illustris-1 are selected in the same way as TNG100. The neutral hydrogen gas mass of a galaxy is also summed up over the gas cells within the radius of 70 kpc.

A nontrivial caveat in the above models is that none of them attempts to actually resolve the neutral phases of the ISM. Thus the predicted neutral hydrogen fraction is not a real prediction based on the ISM chemistry but a modeling related to the effective equation of state function where star formation is initiated once the gas density $n > 0.13\ \mathrm{cm}^{-3}$.

3. Results

3.1. Total Neutral Hydrogen in Simulations and Real Galaxies

Figure 1 shows the neutral hydrogen (H I + H_2) gas mass versus SFR for massive central disk galaxies ($10^{10.6} < M_\star/M_\odot < 10^{11}$) in TNG100, EAGLE, Illustris, L-Galaxies, and observations (Z19). In those four models, notably different black hole feedback models were implemented.

First, all simulations except for EAGLE reproduce well the observed neutral hydrogen gas content for the galaxies with largest SFRs, while EAGLE predicts about 0.3 dex less gas than observed. With SFR decreasing, only TNG100 roughly reproduces the Z19 observational trend (which is also shown by the results in Figure 2), although the scatter around the median relation is not very small. By contrast, galaxies in EAGLE, L-Galaxies, and Illustris are too gas-poor at fixed SFR. When $10^{-0.5} < \mathrm{SFR}/(M_\odot\ \mathrm{yr}^{-1}) < 10^{0.5}$, the neutral hydrogen gas decreases too fast in EAGLE, L-Galaxies, and Illustris, compared to observations and TNG100. For $\mathrm{SFR} < 10^{-0.5}\,M_\odot\ \mathrm{yr}^{-1}$, the neutral hydrogen gas keeps decreasing rapidly in EAGLE, Illustris, and L-Galaxies, and becomes significantly below the observed values (with either the Hα/D_{4000} or UV+IR SFR estimator). We also explored an additional semianalytic model, Shark (Lagos et al. 2018), and found it behaves similarly to Illustris and EAGLE (not shown here to avoid overcrowding of lines). Since the change in gas as SFR decreases in simulations is mainly driven by the implemented AGN feedback model for galaxies in this stellar mass range, the results in Figure 1 suggest that the AGN feedback during quenching might be too efficient in heating/expelling gas from the galaxies in EAGLE, L-Galaxies, and Illustris.

There is a concern on the Z19 observation result that if a different SFR estimator (UV+IR instead of H_α/D_{4000}) is used, the lowest SFRs of central disks are around $\log\mathrm{SFR} = -0.5$ whereas they go down to ~ -1 in the former case. So, these galaxies appear having more or less progressed toward full quenching, depending on the adopted SFR diagnostics (see Figure 1 in Cortese et al. 2020, hereafter C20). The effect of using alternative SFR estimator has been discussed in detail in Z21. The general trends of gas content and other galaxy properties with respect to SFR hold for both SFR estimators. It should also be noted that "disk" galaxies are defined in a very different way in Z19 & Z21 (visual classification by galaxy Zoo) and C20 (a threshold in B/T). These two selections result in very different populations. As shown in Z21, the visually defined disk galaxies with low SFR often have massive bulges, and many of them will be classified as ellipticals using B/T; while most S0s have been classified as ellipticals (or uncertains) in galaxy Zoo, but will be classified as discs by B/T. This different disk selection leads to the fact that the UV+IR derived SFRs in Z19 do not extend to the SFRs as low as in Cortese et al. (2020).

One issue in observation is that the SFRs derived from the SED fitting of UV, optical, and mid-IR bands (Salim et al. 2016, 2018) used in Z19 and Z21, and the UV+IR SFRs used in Cortese et al. (2020) are not corrected for contamination by AGN or hot old stars. Z21 shows almost 100% of the massive discs with the lowest SFRs (by either SFR estimator) host LINERs. Thus the UV+IR SFRs are likely to be the upper limits, and true SFRs could reach lower SFRs. One could subtract off an AGN component by doing the SED decomposition, but this is a very uncertain procedure. For these LINERs, Z19 and Z21 used the SFRs derived from D_{4000}, while such derivation is calibrated with non-AGN galaxies (Brinchmann et al. 2004). Apparently, SFRs from both estimators contain uncertainties at the low-SFR end (dominated by LINERs). Therefore, in our comparison analysis, we use the results derived from both SFR estimators. As shown in Figure 1, the approximate agreement between TNG100 and either SFR estimator holds.

3.2. H I and H_2 Contents (in TNG100)

3.2.1. $M_{H\ I}$ and M_{H_2} versus SFR

Given that TNG100 agrees the best with the observed neutral hydrogen mass–SFR relation, in Figure 2 we show the H I and H_2 gas mass as a function of SFR for these massive central disk galaxies in TNG100, for the five different H I/H_2 decomposition models described in Section 2. In each panel, we show the results for SFRs derived within the entire subhalo (square) and $2R_\star$ (cross) to check the possible influence of varying apertures. It is evident from Figure 2 that above the SFR resolution limits (the vertical dashed line in each panel), all five of these H I/H_2 decomposition models show qualitatively similar trends. That

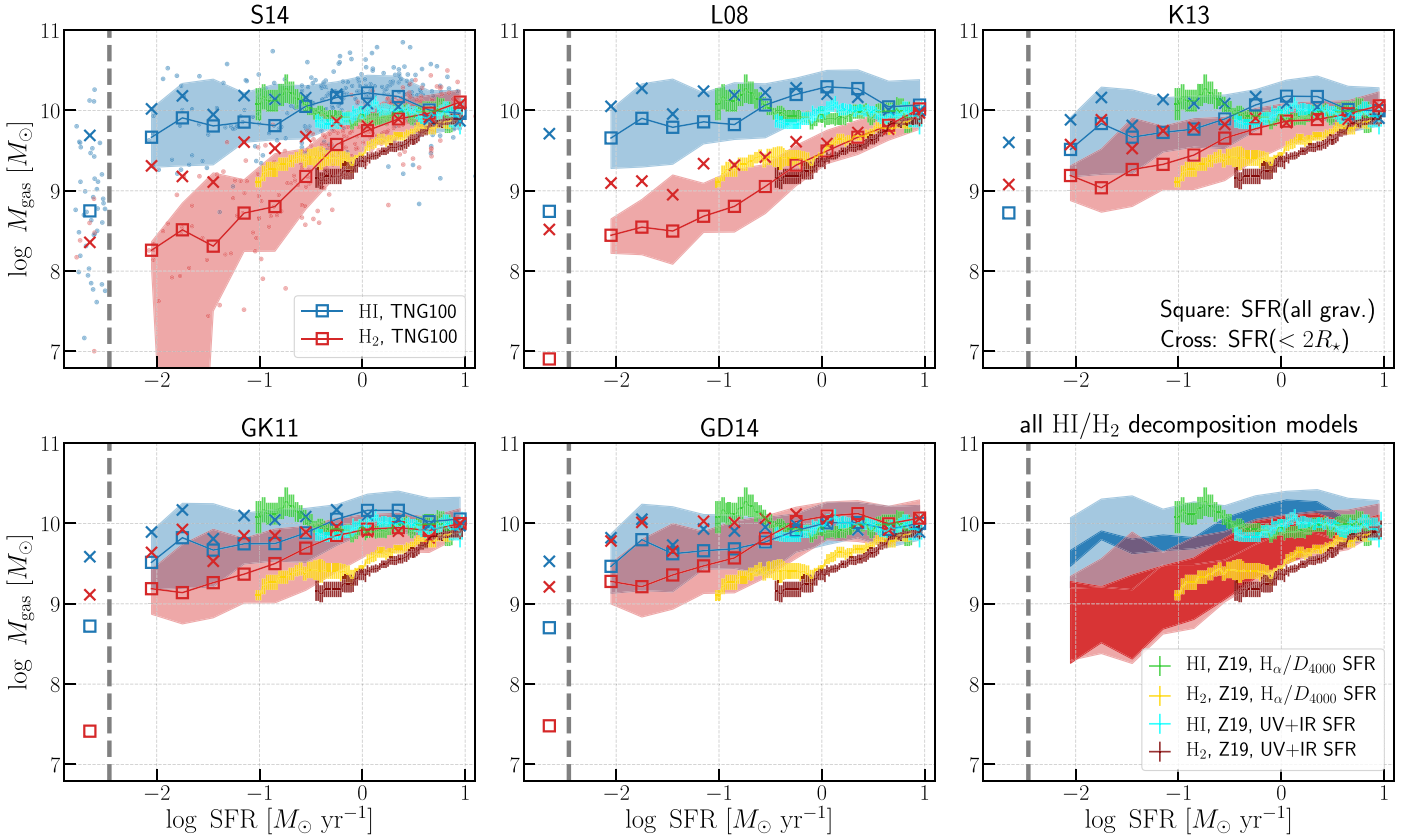

Figure 2. Atomic (H I, blue) and molecular (H_2, red) hydrogen mass vs. SFR in massive central disk galaxies in TNG100. The squares show the median relation for a 200 Myr historical SFR that is summed up over all the star particles gravitationally bound to a galaxy, i.e., to the subhalo; the crosses are the median relation based on particles within $2R_\star$. The shaded areas indicate the 16th–84th percentile ranges. The first five panels show the results from five H I/H_2 decomposition models, as discussed in Section 2. The small dots in the first panel show the distribution of individual galaxies in this massive central disk sample and are not shown in other panels for clarity. The lime green (H I) and gold (H_2) lines are the sliding medians from the observational results of Z19, where SFR is calculated using aperture corrected $H\alpha/D_{4000}$ emission from the SDSS fiber spectra. The observational results using SFRs calculated from SED fitting of UV+IR bands (i.e., Figure 6 of Z19) are overplotted. The gray vertical dashed lines are the SFR resolution limits. We also overplot lines of fixed star formation efficiency $\epsilon = \mathrm{SFR}/M_{\mathrm{gas}}$ for 1 Gyr^{-1}, 0.1 Gyr^{-1}, and 0.01 Gyr^{-1}. In the last panel, the light blue and red shaded areas show the 16th–84th percentile range of the H I and H_2 gas components from all decomposition models for SFR(all grav.), and the darker areas indicate the range of the median relations of the five models.

is, during the quenching of these massive central disk galaxies, as their SFRs decreases, their H_2 gas masses and star formation efficiencies drop but their H I gas masses remain about constant. These trends are in general agreement with those reported by Z19. The results from S14 and L08 models match the observations remarkably well. Nevertheless, given the large systematic uncertainties in the postprocessing (Diemer et al. 2018), we avoid stressing the performance of any individual model but show the variation of all five models in the last panel in Figure 2. It is important to notice that the H_2 mass–SFR relation is more affected by the choices of aperture size. If the SFR($<2R_\star$) is used, in some H I/H_2 decomposition models, the H_2 gas stays roughly unchanged with decreasing SFR. This indicates the existence of a population of galaxies with a good amount of SF outside $2R_\star$ in IllustrisTNG. The observed aperture corrected H_α/D_{4000} SFR and UV+IR SFR represent more the SFR over the whole galaxies including the outer region, thus we take SFR(all grav.) as our default SFR choice. The relations of H I and H_2 mass with SFR agree with the observations within model uncertainties. We further test our results with SFRs calculated using varying apertures and timescales, which is shown in Appendix B.

We note that for galaxies with SFR below the resolution limit, their median H I gas mass is still large, with a median $M_{\mathrm{H\,I}}$ larger than $10^{8.6}\,M_\odot$ when SFR($<2R_\star$) is used and larger than $10^{9.6}\,M_\odot$ when SFR(all grav.) is used, but in general is lower than those with SFR above the limit in all five models. As shown in the figure, observations do not extend to such low SFR. Hence the existence of these fully quenched massive central disk galaxies with a good amount but lower H I gas mass becomes a prediction that can be observationally tested by future deeper H I surveys.

The morphology (i.e., disk galaxies) is measured in a different way in the simulations compared to observations. In Appendix A, we show that the cold gas–SFR relation in TNG100 and EAGLE is almost independent of the morphology, implying that the morphology parameter is irrelevant in interpreting the trends in Figures 1 and 2 when compared with observations. However, the independence (or weak dependence) of the H I mass on morphology clearly contradicts observations. Using the same sample selection, Z19 shows that massive central disk galaxies have an average H I detection fraction of >90%, while the H I detection fraction of massive central elliptical galaxies is only <20%. AGN feedback by itself does not necessarily directly change the morphology. Therefore, the disagreement between observation and simulation may be due to the gas having not been properly processed during morphological transformation in the simulations, such as when mergers and interactions occur.

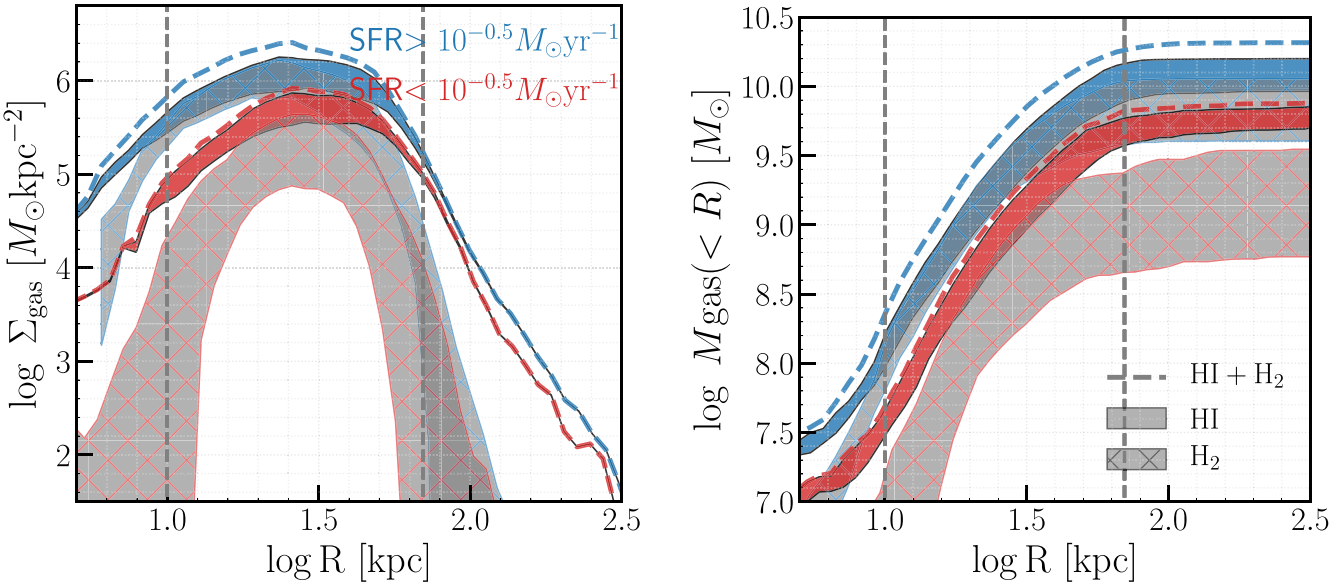

Figure 3. The surface density (face-on) and cumulative radial mass distribution of neutral hydrogen (dashed lines), H I (shaded area), and H_2 (netted shaded region) for higher SFR (blue) and lower SFR (red) central disk galaxies in TNG100, as indicated by the label. The shaded regions indicate the range of median profiles of five H I/H_2 decomposition models. The vertical gray dashed lines correspond to radii of 10 kpc and 70 kpc and are plotted to guide the eye.

The star formation efficiency $\epsilon \equiv \mathrm{SFR}/M_{\rm gas}$ is a widely used observable quantity to explore star formation and quenching in galaxies. ϵ (of the total neutral hydrogen gas) in EAGLE and Illustris is approximately constant at $0.5\,\mathrm{Gyr}^{-1}$, meaning quenching in massive central galaxies in EAGLE and Illustris is primarily driven by the decrease in cold gas. Similarly, in L-Galaxies, ϵ is approximately constant for galaxies with $\mathrm{SFR} > 10^{-0.5}\,M_\odot\ \mathrm{yr}^{-1}$ and then drops rapidly for the most quenched galaxies. Hence quenching in L-Galaxies is first driven by the decrease in the cold gas (with a constant ϵ) and then followed by the decrease in ϵ. In TNG100, as the SFR drops by ∼3 dex, the total neutral hydrogen gas mass drops by ∼0.5 dex and hence ϵ drops by ∼2.5 dex. Therefore, quenching in TNG100 is mainly driven by a decrease in the SF efficiency of the total neutral hydrogen gas. It should be noted that this conclusion relates to the total neutral hydrogen gas and hence does not contradict the result regarding H_2 gas shown in Figure 2 (and also in Dou et al. 2021a, 2021b) that quenching is driven by the decrease in both the H_2 gas mass and H_2 star formation efficiency ϵ_{H_2}. It is straightforward to show that

$$\epsilon_{\mathrm{H\,I+H_2}} = \epsilon_{H_2}/(1 + M_{\mathrm{H\,I}}/M_{H_2}). \quad (1)$$

The decrease in ϵ_{H_2} is smaller than that in $\epsilon_{\mathrm{H\,I+H_2}}$, and the exact amount depends on $M_{\mathrm{H\,I}}/M_{H_2}$. Meanwhile, we stress that in TNG100 the instantaneous SFR in the modeling is calculated based on the local gas density, not based on the H_2 gas density (which is calculated in postprocessing). The dramatic decrease in the $\epsilon_{\mathrm{H\,I+H_2}}$ of ∼2.5 dex during quenching in TNG100 is caused by the decrease in the gas density likely as a consequence of black hole feedback. Note that in TNG100, when the gas density falls below the minimum threshold (i.e., $0.13\,\mathrm{cm}^{-3}$), star formation halts by construction in the simulation.

We suspect that the large differences in the cold-gas content and ϵ during quenching are mainly caused by the different black hole feedback models implemented in IllustrisTNG (kinetic winds), EAGLE (thermal feedback), Illustris (thermal bubble model) and L-Galaxies (preventive feedback). In many semianalytic models, such as L-Galaxies, when the average heating rate from BH feedback exceeds the gas cooling rate in the halo, cold-gas accretion stops and star formation is quenched. The decrease in the cold gas amount during quenching in central discs in L-Galaxies is caused by the heating from the BH, which reduces the cooling rate of the gas. In EAGLE, the BH feedback heats up the ambient gas by a temperature increment of $10^{8.5}$ K; this thermal injection creates a pressure gradient that can produce an outflow. However, this feedback mode might be overly aggressive in heat up cold gas (Davé et al. 2020; Mitchell et al. 2020), resulting in a deficiency of the neutral hydrogen gas. The overall energy injected by BH feedback is similar in IllustrisTNG and Illustris, but the implementation is very different (Pillepich et al. 2018b). The thermal bubble model (Sijacki et al. 2007) in Illustris expels very large amounts of gas from the halo in massive galaxies. The improved kinetic winds (Weinberger et al. 2017) in IllustrisTNG still remove large quantities of gas from galaxies during quenching (see related discussions in Stevens et al. 2019b, 2021; Terrazas et al. 2020) but retain more gas on average, as shown in Figure 1 and Figure 3. We will further discuss the effect of BH feedback in IllustrisTNG on gas properties later.

3.2.2. Gas Distribution Profiles

Given the fact that TNG100 approximately reproduces the average cold gas mass–SFR relation as shown in Figures 1 and 2, we further explore in TNG100 the cold-gas distributions in galaxies with higher $\mathrm{SFR(all\ grav.)} > 10^{-0.5}\ M_\odot\ \mathrm{yr}^{-1}$ and lower $\mathrm{SFR_{limit}} < \mathrm{SFR(all\ grav.)} < 10^{-0.5}\ M_\odot\ \mathrm{yr}^{-1}$, to understand the cause of these relations. In the analysis here we exclude the galaxies with the SFR below the resolution limit. Current observations in cold gas do not extend to such low SFRs; hence the gas properties in this regime remain a prediction from IllustrisTNG to be tested by future deeper surveys.

Figure 3 shows the median surface density profile and the median cumulative radial distributions of the total neutral

hydrogen gas (H I + H_2), H I, and H_2 for galaxies with higher and lower SFRs in TNG100. The two vertical dashed lines mark radii of 10 kpc and 70 kpc to guide the eye. Comparing the total neutral hydrogen gas distribution of galaxies with higher and lower SFR, the difference between the blue and red dashed line is ∼0.9 dex (∼0.7 dex) in the inner regions at ∼10 kpc, and 0.2 dex (∼0.5 dex) in the outer regions at ∼70 kpc for the surface density and cumulative mass. The H_2 surface density profile and cumulative mass profiles of galaxies with SFR(all grav.) $> 10^{-0.5}$ $M_\odot$ yr^{-1} are similar to those in H I, in particular in the inner regions within 30 kpc. By contrast, the H_2 gas masses of galaxies with SFR(all grav.) $> 10^{-0.5}$ $M_\odot$ yr^{-1} are significantly lower than their H I at all radii. The average H I gas within 70 kpc is $\sim 10^{10}$ $M_\odot$ for lower-SFR galaxies and $\sim 10^{9.65}$ $M_\odot$ for higher FSR galaxies. This difference (∼0.35 dex) is smaller than the difference in the total neutral hydrogen gas, which is ∼0.5 dex at this radius. This makes sense in light of the flat $M_{\rm H\,I}$–SFR relation shown in Figure 2.

The significant decrease in the total neutral hydrogen in the central regions of lower-SFR galaxies compared to that of the higher-SFR galaxies is likely due to the BH-driven kinetic feedback in IllustrisTNG (Terrazas et al. 2020). The kinetic winds in IllustrisTNG are implemented by giving the gas immediately surrounding the black hole a momentum kick in a random direction away from the black hole (Weinberger et al. 2017). The kinetic wind generated is isotropic at the injection scales; it impacts the gas not only in the biconical regions but also in the disk. This kinetic wind quenches galaxy SF by both pushing gas out of galaxies (i.e., ejective) and also heating up the gas (i.e., preventive), more so in the central regions (Terrazas et al. 2020; Truong et al. 2020; Zinger et al. 2020). Since H_2 is mainly located in the galaxies' centers, it is the most affected gas phase. While central H I is also decreased, the majority of H I—which lies in the outskirts of galaxies—is less affected. The deficiency of cold gas in the central regions of the lower-SFR galaxies is in agreement with Z19's observations that the central regions of the disk galaxies with lower SFR have $H\alpha/H\beta$ close to the intrinsic value of 3.1, which indicates that there is little dust and gas there. Hence Figure 3 is in fact an important prediction from TNG100, which can be observationally tested with spatially resolved H I and H_2 observations for both star-forming galaxies and those in the process of being quenched.

Interestingly, at any given radius, the H_2 gas mass difference between lower-SFR and higher-SFR galaxies is significantly larger than their H I gas mass difference, indicating that the quenching mechanism, i.e., BH feedback, affects H_2 more (at the same radius). One important result here is that even in the inner regions of the lowest-SFR galaxies, there is a lower but still significant amount of cold gas. Therefore, the quenching (i.e., decrease in the SFR) is mainly caused by the fact that most of this neutral hydrogen gas is in the form of non-star-forming H I, not H_2, which leads to the very low ϵ of the total neutral hydrogen gas, as discussed above. As shown in Diemer et al. 2018, for all of the five H I/H_2 decomposition models, the fraction of neutral hydrogen that is H_2 depends steeply on the gas density in a certain range (see also Morselli et al. 2020). The removal of the high-density gas due to feedback can have a stronger effect on H_2 than H I, leading to the low H_2-to-H I ratio, as shown here in Figure 3 and also in Figure 2. In Appendix C, we show the stellar light and total gas distribution for two typical central disk galaxies in TNG100, one with SFR(all grav.) $> 10^{-0.5}$ $M_\odot$ yr^{-1} and one with SFR(all grav.) $< 10^{-0.5}$ $M_\odot$ yr^{-1}, to give a more direct view on the above discussion.

4. Discussion and Summary

Recent observations indicate the ubiquitous existence of large regularly rotating H I discs in massive central disk galaxies, both in those that are star-forming and in those in the process of being quenched (Z19). This result has yet been used to calibrate the recipes in the hydrodynamical simulations and semianalytic models and can therefore serve as a new observational test of these simulations, in particular of their AGN feedback models, as the existence of an H I disk at high stellar masses requires the strength and modes of AGN feedback to be just right. If feedback is too violent, H I discs will not survive during quenching; if it is too weak, it will not be able to deplete the H_2 gas in the galaxy and to quench the star formation.

Among the simulations we tested, only TNG100 of the IllustrisTNG project appears to approximately reproduce the trend in cold gas versus the SFR, as reported in Z19, and some H_2/H I decomposition method may even reproduce the observed H_2 and H I trends separately. This lends some support to the AGN feedback implementation in TNG100, though other factors may also be at play. Given the coarse resolution of cosmological hydro simulation relative to the high-resolution simulation of individual galaxy that can resolve the Bondi radius (Yuan et al. 2015, 2018) and the subgrid nature of the the AGN feedback models implemented, it is difficult to derive too much detail about the AGN feedback physics. However, reproducing the observed gas content of galaxies of various properties will be critical for future development in cosmological simulations. Also, the fact that none of the models tested in this work reproduce the morphology–HI gas mass relation challenges the current models.

In IllustrisTNG, the kinetic winds drive outflows that push gas out of galaxies (Nelson et al. 2019a) and increase the gas entropy (Zinger et al. 2020), more so in the central regions, while the H I gas at larger radii ($\gtrsim$30 kpc) is less affected. This explains the relatively flat $M_{\rm H\,I}$–SFR relation shown in Figure 2. Meanwhile, the kinetic feedback also leads to a sharp decrease in gas density, which then leads to a sharp decrease in the fraction of molecular hydrogen computed in the decomposition models (see Stevens et al. 2021). This explains the rapid decrease in the H_2 gas mass and SFR during quenching. The simultaneous role of being ejective and preventive for AGN feedback in IllustrisTNG also implies that cold-gas accretion during quenching is strangulated. These results are also in qualitative agreement with those derived from the observed SFR/$M_\star$–$M_{\rm H_2}/M_\star$–SFR/$M_{\rm H_2}$ scaling relations (Dou et al. 2021b), in that to quench massive galaxies, strangulation plus additional H_2 gas removal (with a mass-loading factor of about unity) are required (Dou et al. 2021a).

It should be noted that the existence of the observed regularly rotating H I disk around the massive central disk galaxies that are undergoing quenching process as in Z19 & Z21, can be explained by AGN feedback as above. Alternatively, it can be caused by angular-momentum quenching as proposed in Peng & Renzini (2020) and Renzini (2020) that the inflowing gas with excess angular momentum can settle on a stable outer neutral hydrogen disk for a long timescale in the absence of perturbation. This is supported by recent studies in simulations, which found that a sufficiently high angular momentum of the circumgalactic medium is an important factor in keeping a galaxy quenched (Lu et al. 2021; Wang et al. 2022). Although AGN feedback must be

important to quench massive galaxies in simulations (e.g., Su et al. 2019) and can well reproduce the observed cold-gas content during quenching, as shown in this paper, it may not be the case in the real universe. We will further investigate both AGN and non-AGN solutions to the quenching of massive galaxies in our future work.

We gratefully acknowledge the anonymous referee for comments and criticisms that have improved the paper.

J.S., Y.P. and L.C.H. acknowledge National Science Foundation of China (NSFC) grant Nos. 12125301, 11773001, 12192222, 11721303, and 11991052, and the National Key R and D Program of China grant No. 2016YFA0400702.

J.S. acknowledges Martina Donnari for providing the SFRs of galaxies in TNG100.

A.R.H.S. acknowledges receipt of the Jim Buckee Fellowship at ICRAR-UWA.

A.R. acknowledges support from the INAF/PRIN-SKA 2017 "ESKAPEHI" grant.

We acknowledge the science research grants from the China Manned Space Project with No. CMS-CSST-2021-A04 and No. CMS-CSST-2021-A07.

Y.G.'s work is partially supported by National Key Basic Research and Development Program of China (grant No. 2017YFA0402704), National Natural Science Foundation of China (NSFC; grant Nos. 12033004, and 11861131007), and Chinese Academy of Sciences Key Research Program of Frontier Sciences (grant No. QYZDJ-SSW-SLH008).

We acknowledge the Virgo Consortium for making their simulation data available. The eagle simulations were performed using the DiRAC-2 facility at Durham, managed by the ICC, and the PRACE facility Curie based in France at TGCC, CEA, Bruyéres-le-Châtel.

R.M. acknowledges an ERC Advanced grant No. 695671 QUENCH, and support from the UK Science and Technology Facilities Council (STFC). R.M. also acknowledges funding from a research professorship from the Royal Society.

Appendix A
Cold Gas–SFR Relation for Centrals in TNG100 and EAGLE

A major concern for the study of the neutral hydrogen gas–SFR relation is the definition of the galaxy morphology; how we choose what constitutes a disk can affect our results. There are various morphology metrics used for both observations and simulations that allow one to distinguish between discs and ellipticals. However, exploring which one is better is not the task of this work. Here we briefly assess the H I gas–SFR relation for ellipticals in TNG100 and EAGLE. As shown in Figure A1, the H I mass for ellipticals is slightly lower but not significantly different from that of discs in TNG100. This is mainly caused by the higher-than-observed H I content of TNG100 ellipticals, as pointed out by Diemer et al. (2019). The independence of the cold-gas content at given SFR with the morphology is also shown in EAGLE, as seen in Figure A2. These results indicate that the neutral hydrogen gas mass–SFR relation shown in the main text is not significantly affected even if the morphological selection of galaxies in the simulations is not perfect.

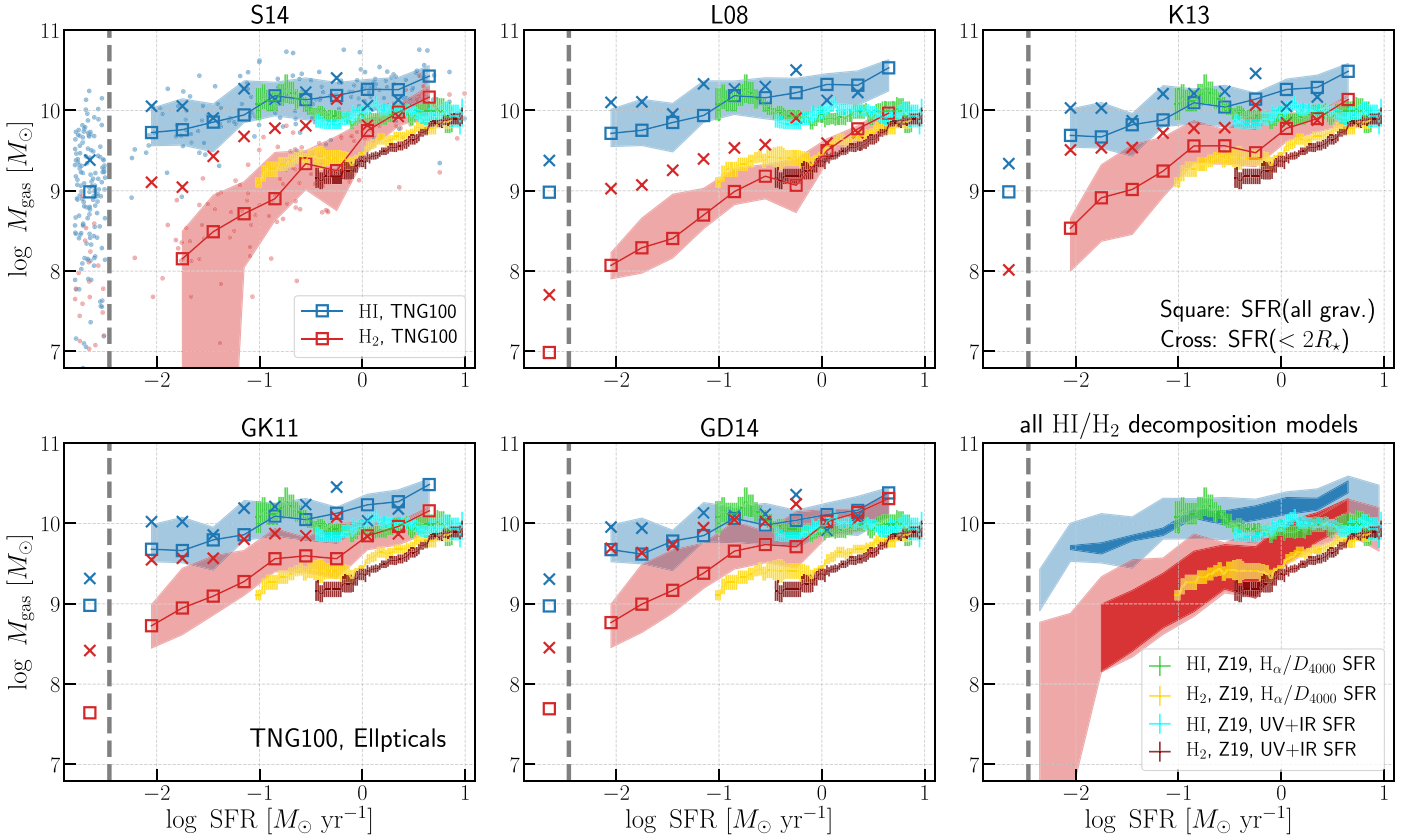

Figure A1. Similar to Figure 2, but for ellipticals in TNG100. Note that here the observations are for central discs.

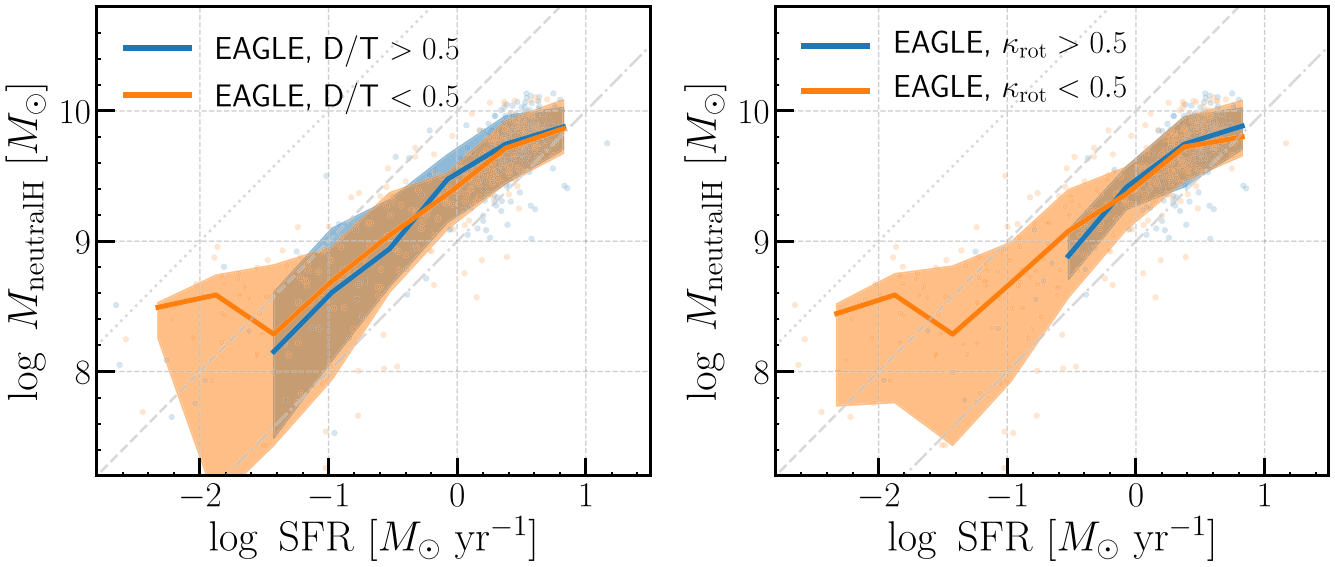

Figure A2. Neutral hydrogen gas mass vs. SFR for central discs and ellipticals in EAGLE. The left- and right-hand panels, respectively, show the morphology divisions using disk-to-total mass ratio (D/T) and rotation support parameter ($\kappa_{\rm rot}$). The blue and oranges lines are median relations for discs and ellipticals separately, together with the 16th–84th percentile ranges shown by the shaded areas.

Appendix B
SFR Over Different Timescales and Apertures

In observations, different SFR indicators, such as UV continuum, Hα emission/D_{4000}, IR continuum, and 1.4 GHz emission, are sensitive to the SFR over different timescales, varying from less than ∼10 Myr for Hα to ∼100 Myr for UV +IR (Speagle et al. 2014). In simulations, SFRs can also be calculated using different timescales and apertures. To test the impact of timescale and aperture choices, in Figure B1, we plot the gas–SFR relation of the L08 model as in Figure 2, but using SFRs derived within different timescales (from instantaneous to

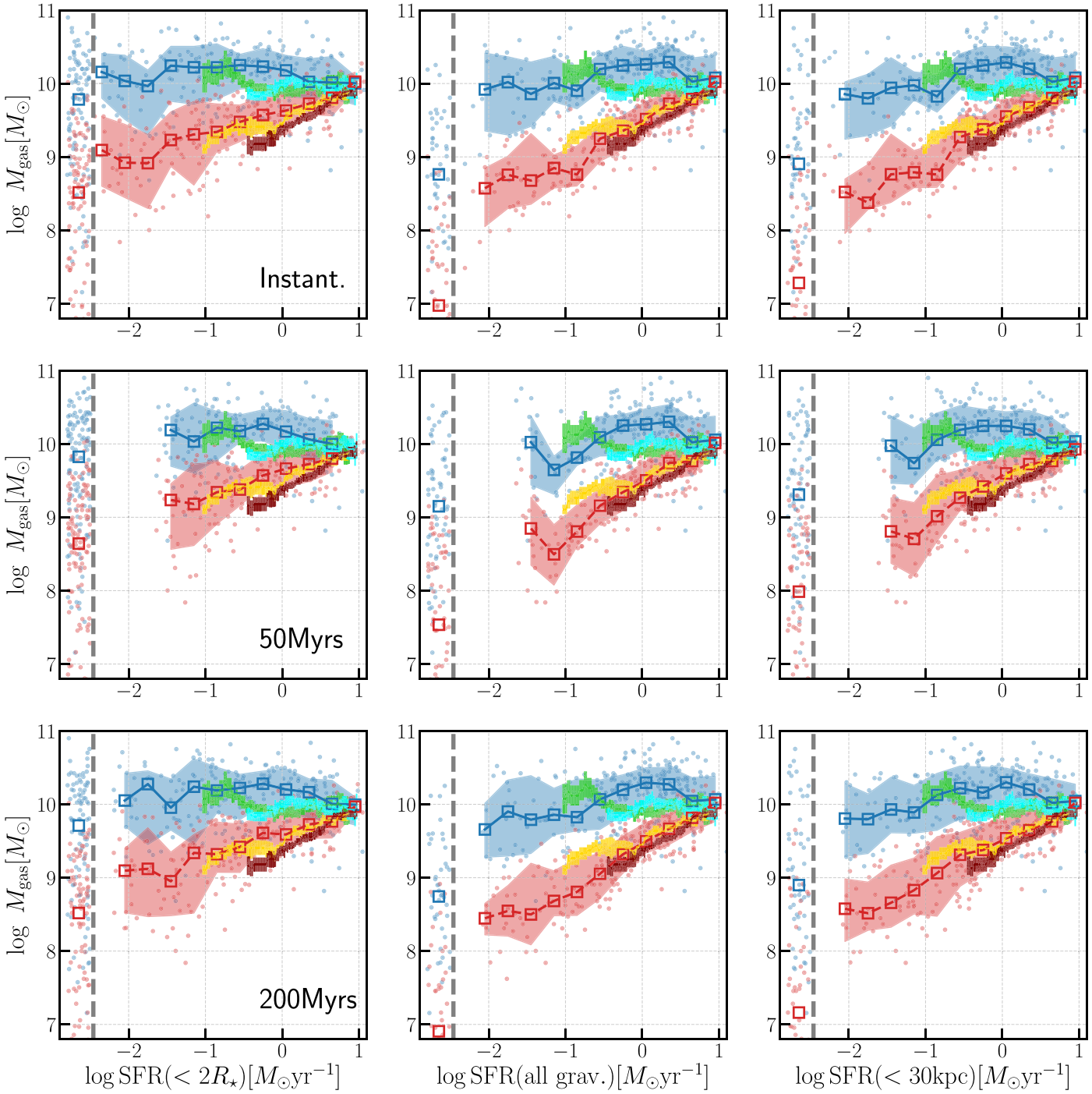

Figure B1. H I and H_2 gas mass vs. SFRs calculated over different timescales and different apertures. TNG100 H I and H_2 masses here use the L08 decomposition model. The lime green and gold lines with error bars are the observational results given in Z19 for H I and H_2 respectively.

200 Myr) and apertures ($<2R_\star$, <30 kpc, all grav.; Donnari et al. 2019). There are differences and variations of the results in different panels, but the general trends for both H I and H_2 remain similar and are in general agreement with observations. We also tested the results derived with other H I/H_2 decomposition models and found that the general trends remain unchanged against SFRs calculated using different apertures and timescales. We want to point out that, while the timescale and aperture choices for the simulation are not particularly important, the SFR indicators used for the observations are still very important, as the modeling uncertainties in observations are more complicated than just timescales and apertures (for example, see the difference between H_α/D_{4000} and UV+IR SFRs as highlighted in Z19).

Appendix C
Gas Density in Example SF and Quenching Galaxies

In Figure C1, we show the stellar light and total gas distribution for a typical higher-SFR central disk galaxy and a lower-SFR central disk in TNG100. The lower-SFR galaxy also shows a regular rotating gas disk, similar to the higher-SFR one. This is also in good agreement with the results

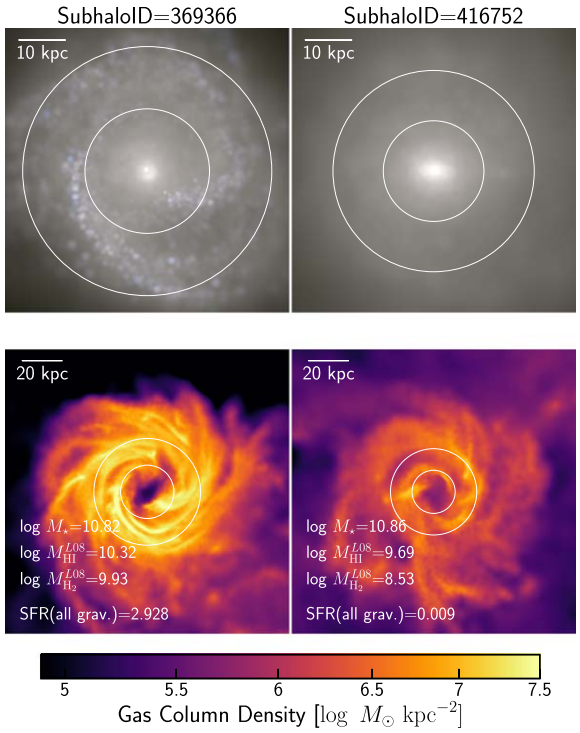

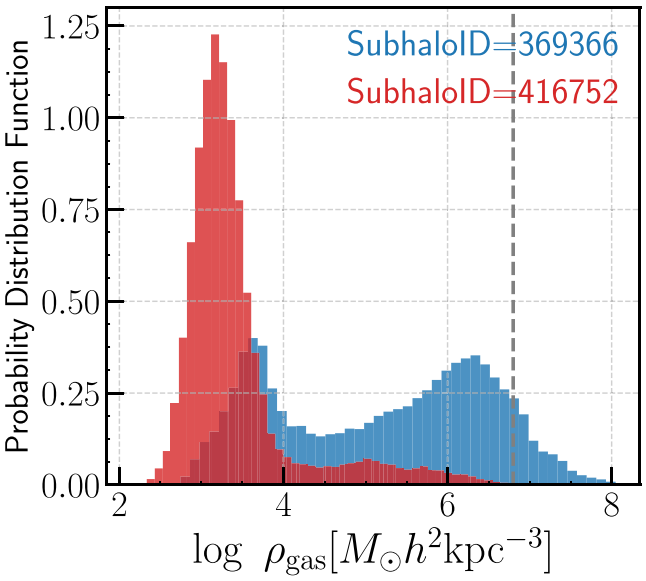

Figure C1. Left: composite stellar light of the James Webb Space Telescope wide bands of F200W+F115W+F070W (upper) and gas (lower) distribution of a representative higher SFR(all grav.) $> 10^{-0.5}$ $M_\odot$ yr^{-1} and a lower SFR$_{\rm limit}$ < SFR(all grav.) $< 10^{-0.5}$ $M_\odot$ yr^{-1} disk galaxy at $z = 0$. The image sizes are 60 kpc × 60 kpc for the stellar light and 140 kpc × 140 kpc for the gas. Galaxies are rotated to be face-on. The circles indicate the $1.0R_\star$ and $2.0R_\star$ radii. Please note that the scale of the color coding for the gas density is the same for both galaxies. Masses and SFRs are in units of $M_\odot$ and $M_\odot$ yr^{-1}, respectively. Right: 3D gas density distribution in the example galaxies in TNG100. The gray vertical line indicates the density threshold for star formation adopted in IllustrisTNG model.

in Z19, where they find that most of the quenching central disk galaxies show characteristically symmetric double-horn H I profiles, indicating regularly rotating H I discs with little significant kinematic perturbations, similar to the star-forming ones. The difference between the two galaxies is more directly shown in the right panel. Comparing to the one with higher SFR, in the lower-SFR galaxy, there are fewer regions with high gas density (hence less gas is in the form of H_2). The dashed line corresponds to a density threshold of 0.13 cm^{-3} (i.e., $n_{\rm H} \sim 0.1$ cm^{-3}) set up for star formation. Note the gas cell volumes in quenching galaxy are much larger than the SF ones; as a result, the surface density profiles of these two galaxies are not significantly different.

ORCID iDs

Jingjing Shi https://orcid.org/0000-0001-9879-4926
Benedikt Diemer https://orcid.org/0000-0001-9568-7287
Annalisa Pillepich https://orcid.org/0000-0003-1065-9274
Alvio Renzini https://orcid.org/0000-0002-7093-7355
Jing Dou https://orcid.org/0000-0002-6961-6378
Qiusheng Gu https://orcid.org/0000-0002-3890-3729
Luis C. Ho https://orcid.org/0000-0001-6947-5846
Xu Kong https://orcid.org/0000-0002-7660-2273
Jiaxuan Li https://orcid.org/0000-0001-9592-4190
Roberto Maiolino https://orcid.org/0000-0002-4985-3819
Filippo Mannucci https://orcid.org/0000-0002-4803-2381
Chengpeng Zhang https://orcid.org/0000-0001-6469-1582

References

Ayromlou, M., Kauffmann, G., Yates, R. M., Nelson, D., & White, S. D. M. 2021, MNRAS, 505, 492
Bahé, Y. M., Yannick, M., Crain, R. A., et al. 2016, MNRAS, 456, 1115
Behroozi, P., Wechsler, R. H., Hearin, A. P., & Conroy, C. 2019, MNRAS, 488, 3143
Benson, A. J., Bower, R. G., Frenk, C. S., et al. 2003, ApJ, 599, 38
Bower, R. G., Benson, A. J., Malbon, R., et al. 2006, MNRAS, 370, 645
Brinchmann, J., Charlot, S., White, S. D. M., et al. 2004, MNRAS, 351, 1151
Calette, A. R., Avila-Reese, V., Rodríguez-Puebla, A., Hernández-Toledo, H., & Papastergis, E. 2018, RMxAA, 54, 443
Catinella, B., Saintonge, A., Janowiecki, S., et al. 2018, MNRAS, 476, 875
Cortese, L., Catinella, B., Cook, R. H. W., & Janowiecki, S. 2020, MNRAS, 494, L42
Crain, R. A., Bahé, Y. M., Lagos, C., et al. 2017, MNRAS, 464, 4204
Crain, R. A., Schaye, J., Bower, R. G., et al. 2015, MNRAS, 450, 1937
Cresci, G., Mainieri, V., Brusa, M., et al. 2015, ApJ, 799, 82
Cresci, G., & Maiolino, R. 2018, NatAs, 2, 179
Croton, D. J., Springel, V., White, S. D. M., et al. 2006, MNRAS, 365, 11
Davé, R., Anglés-Alcázar, D., Narayanan, D., et al. 2019, MNRAS, 486, 2827
Davé, R., Crain, R. A., Stevens, A. R. H., et al. 2020, MNRAS, 497, 146
Davis, M., Efstathiou, G., Frenk, C. S., & White, S. D. M. 1985, ApJ, 292, 371
Diemer, B., Stevens, A. R. H., Forbes, J. C., et al. 2018, ApJS, 238, 33
Diemer, B., Stevens, A. R. H., Lagos, C. d. P., et al. 2019, MNRAS, 487, 1529
Donnari, M., Pillepich, A., Nelson, D., et al. 2019, MNRAS, 485, 4817
Dou, J., Peng, Y., Renzini, A., et al. 2021a, ApJ, 915, 94
Dou, J., Peng, Y., Renzini, A., et al. 2021b, ApJ, 907, 114
Dutton, A. A., Conroy, C., van den Bosch, F. C., Prada, F., & More, S. 2010, MNRAS, 407, 2
Gallagher, R., Maiolino, R., Belfiore, F., et al. 2019, MNRAS, 485, 3409
Genel, S., Vogelsberger, M., Springel, V., et al. 2014, MNRAS, 445, 175
Gnedin, N. Y., & Draine, B. T. 2014, ApJ, 795, 37
Gnedin, N. Y., & Kravtsov, A. V. 2011, ApJ, 728, 88
Guo, Q., White, S., Boylan-Kolchin, M., et al. 2011, MNRAS, 413, 101
Henriques, B. M. B., White, S. D. M., Thomas, P. A., et al. 2015, MNRAS, 451, 2663
Henriques, B. M. B., Yates, R. M., Fu, J., et al. 2020, MNRAS, 491, 5795
Ishibashi, W., & Fabian, A. C. 2012, MNRAS, 427, 2998
Jones, M. G., Haynes, M. P., Giovanelli, R., & Moorman, C. 2018, MNRAS, 477, 2
Kravtsov, A. V., Vikhlinin, A. A., & Meshcheryakov, A. V. 2018, AstL, 44, 8
Krumholz, M. R. 2013, MNRAS, 436, 2747

Lagos, C. d. P., Crain, R. A., Schaye, J., et al. 2015, MNRAS, 452, 3815
Lagos, C. d. P., Tobar, R. J., Robotham, A. S. G., et al. 2018, MNRAS, 481, 3573
Larson, R. B. 1974, MNRAS, 169, 229
Leroy, A. K., Walter, F., Brinks, E., et al. 2008, AJ, 136, 2782
Lu, S., Xu, D., Wang, S., et al. 2021, MNRAS, 509, 2707
Maiolino, R., Russell, H. R., Fabian, A. C., et al. 2017, Natur, 544, 202
Marinacci, F., Vogelsberger, M., Pakmor, R., et al. 2018, MNRAS, 480, 5113
McAlpine, S., Helly, J. C., Schaller, M., et al. 2016, A&C, 15, 72
Mitchell, P. D., Schaye, J., Bower, R. G., & Crain, R. A. 2020, MNRAS, 494, 3971
Morselli, L., Rodighiero, G., Enia, A., et al. 2020, MNRAS, 496, 4606
Moster, B. P., Naab, T., & White, S. D. M. 2018, MNRAS, 477, 1822
Naab, T., & Ostriker, J. P. 2017, ARA&A, 55, 59
Naiman, J. P., Pillepich, A., Springel, V., et al. 2018, MNRAS, 477, 1206
Nelson, D., Pillepich, A., Genel, S., et al. 2015, A&C, 13, 12
Nelson, D., Pillepich, A., Springel, V., et al. 2018, MNRAS, 475, 624
Nelson, D., Pillepich, A., Springel, V., et al. 2019a, MNRAS, 490, 3234
Nelson, D., Springel, V., Pillepich, A., et al. 2019b, ComAC, 6, 2
Pawlik, A. H., & Schaye, J. 2008, MNRAS, 389, 651
Peng, Y.-J., & Renzini, A. 2020, MNRAS, 491, L51
Pillepich, A., Nelson, D., Hernquist, L., et al. 2018a, MNRAS, 475, 648
Pillepich, A., Springel, V., Nelson, D., et al. 2018b, MNRAS, 473, 4077
Rahmati, A., Pawlik, A. H., Raičević, M., & Schaye, J. 2013, MNRAS, 430, 2427
Rees, M. J., & Ostriker, J. P. 1977, MNRAS, 179, 541
Renzini, A. 2020, MNRAS, 495, L42
Rodriguez-Gomez, V., Genel, S., Vogelsberger, M., et al. 2015, MNRAS, 449, 49
Saintonge, A., Catinella, B., Cortese, L., et al. 2016, MNRAS, 462, 1749
Sales, L. V., Navarro, J. F., Theuns, T., et al. 2012, MNRAS, 423, 1544
Salim, S., Boquien, M., & Lee, J. C. 2018, ApJ, 859, 11
Salim, S., Lee, J. C., Janowiecki, S., et al. 2016, ApJS, 227, 2
Schaye, J., Crain, R. A., Bower, R. G., et al. 2015, MNRAS, 446, 521
Sijacki, D., Springel, V., Di Matteo, T., & Hernquist, L. 2007, MNRAS, 380, 877
Sijacki, D., Vogelsberger, M., Genel, S., et al. 2015, MNRAS, 452, 575
Silk, J. 2003, MNRAS, 343, 249
Silk, J. 2013, ApJ, 772, 112
Silk, J., & Rees, M. J. 1998, A&A, 331, L1
Somerville, R. S., & Davé, R. 2015, ARA&A, 53, 51
Speagle, J. S., Steinhardt, C. L., Capak, P. L., & Silverman, J. D. 2014, ApJS, 214, 15
Springel, V. 2010, MNRAS, 401, 791
Springel, V., & Hernquist, L. 2003, MNRAS, 339, 289
Springel, V., White, S. D. M., Tormen, G., & Kauffmann, G. 2001, MNRAS, 328, 726
Springel, V., Pakmor, R., Pillepich, A., et al. 2018, MNRAS, 475, 676
Sternberg, A., Le Petit, F., Roueff, E., & Le Bourlot, J. 2014, ApJ, 790, 10
Stevens, A. R. H., Diemer, B., Lagos, C. D. P., et al. 2019a, MNRAS, 490, 96
Stevens, A. R. H., Diemer, B., Lagos, C. d. P., et al. 2019b, MNRAS, 483, 5334
Stevens, A. R. H., Lagos, C. d. P., Cortese, L., et al. 2021, MNRAS, 502, 3158
Su, K.-Y., Hopkins, P. F., Hayward, C. C., et al. 2019, MNRAS, 487, 4393
Tacconi, L. J., Genzel, R., Saintonge, A., et al. 2018, ApJ, 853, 179
Terrazas, B. A., Bell, E. F., Pillepich, A., et al. 2020, MNRAS, 493, 1888
Torrey, P., Vogelsberger, M., Genel, S., et al. 2014, MNRAS, 438, 1985
Truong, N., Pillepich, A., Werner, N., et al. 2020, MNRAS, 494, 549
Vogelsberger, M., Genel, S., Sijacki, D., et al. 2013, MNRAS, 436, 3031
Vogelsberger, M., Genel, S., Springel, V., et al. 2014, Natur, 509, 177
Wang, L., & Jing, Y. P. 2010, MNRAS, 402, 1796
Wang, S., Xu, D., Lu, S., et al. 2022, MNRAS, 509, 3148
Wechsler, R. H., & Tinker, J. L. 2018, ARA&A, 56, 435
Weinberger, R., Springel, V., Hernquist, L., et al. 2017, MNRAS, 465, 3291
White, S. D. M., & Frenk, C. S. 1991, ApJ, 379, 52
White, S. D. M., & Rees, M. J. 1978, MNRAS, 183, 341
Yang, X., Mo, H. J., & van den Bosch, F. C. 2009, ApJ, 695, 900
Yang, X., Mo, H. J., van den Bosch, F. C., Zhang, Y., & Han, J. 2012, ApJ, 752, 41
Yates, R. M., Henriques, B., Thomas, P. A., et al. 2013, MNRAS, 435, 3500
Yuan, F., Gan, Z., Narayan, R., et al. 2015, ApJ, 804, 101
Yuan, F., & Narayan, R. 2014, ARA&A, 52, 529
Yuan, F., Yoon, D., Li, Y.-P., et al. 2018, ApJ, 857, 121
Zhang, C., Peng, Y., Ho, L. C., et al. 2019, ApJL, 884, L52
Zhang, C., Peng, Y., Ho, L. C., et al. 2021, ApJ, 911, 57
Zheng, Z., Coil, A. L., & Zehavi, I. 2007, ApJ, 667, 760
Zinger, E., Pillepich, A., Nelson, D., et al. 2020, MNRAS, 499, 768
Zubovas, K., Nayakshin, S., King, A., & Wilkinson, M. 2013, MNRAS, 433, 3079